Check for updates

IET Power Electronics

WILEY

The Institution of Engineering and Technology

ORIGINAL RESEARCH OPEN ACCESS

Robust Deadbeat-Based Current Control for High Pole Count Machines in Flux Weakening Region

Emilio Carfagna[1] | Fabio Bernardi[2] | Giovanni Migliazza[1] | Emilio Lorenzani[1,3]

[1]Department of Science and Methods for Engineering, University of Modena and Reggio Emilia, Reggio Emilia, Italy | [2]Department of Engineering "Enzo Ferrari", University of Modena and Reggio Emilia, Modena, Italy | [3]InterMech–MO.RE., University of Modena and Reggio Emilia, Modena, Italy

Correspondence: Emilio Carfagna (emilio.carfagna@unimore.it)

Received: 19 February 2026 | **Revised:** 4 August 2026 | **Accepted:** 9 September 2026

ABSTRACT

High pole count machines offer high torque density, making them suitable for various industrial applications. Closed-loop field-oriented control is commonly used to maximize the efficiency and dynamic performance of sensored drives. Furthermore, flux weakening can extend the operational speed range, leveraging the lower short-circuit current characteristic of these motors (that is lower than the nominal one), although this feature is often underutilized. This work introduces a new deadbeat current control method designed to overcome the limitations of modulated model predictive control. The approach enhances robustness against electrical parameter errors and dead-time effects. Simulation and experimental results are presented from a low-power hybrid stepper motor with a high number of rotor teeth, showcasing the benefits of the proposed control in terms of extended speed range and improved dq current tracking.

1 | Introduction

High pole count machines offer increased motor torque capacity [1]. Examples include direct drive motors (or torque motors) [2] and hybrid stepper motors (HSMs) [3]. A limitation of these machines is the high maximum electrical frequency, f_{el}, encountered in the middle-to-high speed range. High-speed drives can be categorized into two types: those with high mechanical speeds, used in applications such as compressors and fans [4], and those with a high number of pole pairs, employed for precision control in applications such as laboratory equipment for accurate dosage [5], micro-surgical manipulations [6], and robotic grippers [7].

For HSMs, the mathematical dq model is the same as a surface permanent magnet synchronous machine (SPMSM), with additional no-idealities as high cogging torque ripple [8, 9] and with a higher capability for flux weakening (FW) thanks to short-circuit current lower than the nominal one [10]. This characteristic is common in case of machines with large winding inductance and consequently an infinite constant power speed ratio [11].

This issue related to high speed region and fast dynamic controls have been widely covered in scientific literature, in particular applying different current controls based on model predictive controls (MPCs) and deadbeat controls. Finite control set-MPC (FCS-MPC) has fast dynamic response with a simple inclusion of multiple objectives and constraints without introducing extra control loops [12]. The application of FCS-MPC on architectures with many states of the inverter is challenging due to the heavy computational burden. Additional issues are the design of output filters due to the variable switching frequency f_{sw} and the presence of high torque ripples since FCS-MPC applies only one vector during the entire control period.

To reduce torque ripples, different MPC strategies are introduced such as continuous control set (CCS)-MPC, which takes actions into a continuous set [13], model-free predictive current control that can avoid reliance on motor parameters [14] and constant switching frequency MPC which is applied to the current control of a three-phase active rectifier [15]. The latter technique allows maintaining the advantages of MPC, ensuring a constant

This is an open access article under the terms of the Creative Commons Attribution License, which permits use, distribution and reproduction in any medium, provided the original work is properly cited.
© 2026 The Author(s). *IET Power Electronics* published by John Wiley & Sons Ltd on behalf of The Institution of Engineering and Technology.

TABLE 1 | Comparison of predictive current control methods under low carrier ratio conditions.

Control method	High electrical frequency	Flux weakening region	Electrical parameters errors	Deadtime influence
CCS-MPC [13]	✓	×	✓	×
M²PC [17]	✓	×	✓	×
Deadbeat PCC [23]	✓	×	✓	✓
Deadbeat PCC [30]	×	×	✓	×
Proposed control	✓	✓	✓	✓

switching frequency of the space vector modulation (SVM) and increasing the performances in terms of power quality. This control strategy, also known as modulated MPC (M²PC), has been applied to PMSMs with low electrical frequency [16] and high-speed PMSMs [17], but the flux weakening region is not studied in case of isotropic motor.

However, M²PC evaluates two active vectors at a time to find the best sector of the SVM, so computational burden is high even with this control.

Contributions evaluating predictive controls on high pole count machines are already known comparing PI, sliding mode control, incremental deadbeat control and FCS-MPC for HSMs [3], but the flux weakening region is not studied. This manuscript has the following goals:

- analysis of M²PCs controls. M²PCs and deadbeat controls for surface-mounted PMSMs are used with $i_d^\star$ equal to 0 and low electrical frequencies (see for example [14, 16, 18–22]). Even with high-speed motors, the PMSM is driven with $i_d^\star$ equal to 0 [13, 17]. Alternatives to classical deadbeat current control for high-speed motors adopt deadbeat with stator flux vector in the stationary frame to achieve the tracking of dq currents [23]. However, the behaviour is outside the FW region. The HSM can be successfully applied in FW region thanks to the large winding inductance and has high electrical frequencies due to the high number of rotor teeth [24]. In this scenario, M²PC shows limitations in FW region due to the simultaneous action of multiple constraints of voltage and current [25];
- proposal of a robust deadbeat control (RDC) able to save computational burden with improved control performance and robustness of M²PC in low speed region and with the ability to extend the speed range in FW region. In [26, 27] the current loops use the conventional deadbeat control and the FW region is addressed modifying the flux weakening controller, whereas [28] proposes a deadbeat-based direct flux vector control (DFVC) for SPMSMs working in FW region. The same approach can be generalized for interior permanent magnet synchronous machines [29]. In this manuscript, an analysis of the impact of the dead-time and of the errors on electrical parameters is exposed and tested during simulations and experimental;
- final comparison on pros and cons of the proposed control with respect to a traditional PI control under low carrier ratio condition. Table 1 reports a comparison between predictive current controls (PCCs) and the proposed strategy under low carrier ratio.

An HSM with 50 rotor teeth is chosen as reference machine for simulations and experimental results. A SVM for two-phase machines is employed [31]. The performance analysis is carried out at standstill considering the step response and the bandwidth of the current loops, whereas when the rotor moves the total harmonic distortion (THD) of the phase currents in FW region and the regulation of the dq currents with high speeds are taken into account.

The paper is organized as follows: Section 2 describes the adopted mathematical model of HSM, whereas Section 3 exhibits the proposed robust deadbeat control with space vector modulation for two-phase machines. Sections 4 and 5 report simulations and experimental results, followed by Conclusions.

2 | Mathematical Model

The dynamic of a two phase hybrid stepper motor in the (d, q) reference frame, according to [3, 24], is given by:

$$\begin{cases} u_d = L_0 \dfrac{di_d}{dt} + R_s i_d - i_q N_r \omega L_0 \\ u_q = L_0 \dfrac{di_q}{dt} + R_s i_q + i_d N_r \omega L_0 + k_M \omega \\ \dot{\theta} = \omega \\ J\dot{\omega} + F\omega = k_M i_q - T_L - T_c \\ T_c = N_r F_m^2 \displaystyle\sum_{j=1}^{m} 4jP_{4j} \sin(4jN_r\theta) \end{cases} \tag{1}$$

where: θ is the (mechanical) rotor angle, ω is the (mechanical) rotor speed, (i_d, i_q) are the stator currents and (u_d, u_q) are the stator voltages. The variables $(\theta, \omega, i_d, i_q)$ are the state variables, while (u_d, u_q) are the control inputs and the load torque T_L is the unknown disturbance input.

The other model parameters are: the viscous friction coefficient F, the number of rotor teeth N_r, the moment of inertia J, the stator winding resistance R_s, the stator inductance L_0 and the torque constant k_M equal to $N_r\Phi_{PM}$ where Φ_{PM} is the flux linkage provided by the permanent magnet.

The term T_c models the disturbance torque due to cogging (F_m is the magneto-motive force of permanent magnet and P_{4j} is the amplitude of the j harmonics [8]). The electrical speed and angle are $\omega_e = N_r\omega$ and $\theta_e = N_r\theta$, respectively. The derivation of the

17554543, 2026, 1, Downloaded from https://ietresearch.onlinelibrary.wiley.com/doi/10.1049/pel2.70318 by CochraneItalia, Wiley Online Library on [22/10/2026]. See the Terms and Conditions (https://onlinelibrary.wiley.com/terms-and-conditions) on Wiley Online Library for rules of use; OA articles are governed by the applicable Creative Commons License

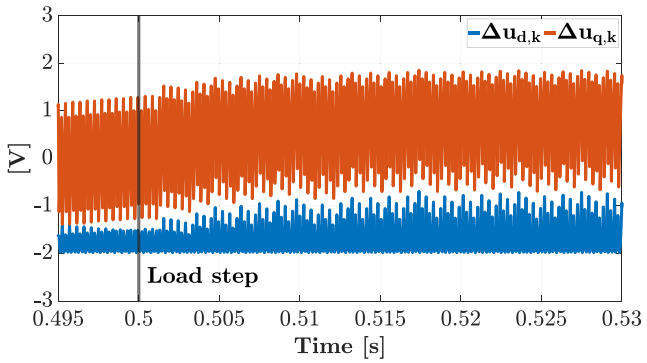


FIGURE 1 | Dead-time voltages with $T_{dt} = 1\,\mu s$ and $V_{DC} = 70$ V in FW region at 140 rad/s with load step from 0 to 1 Nm.

model above is obtained under the assumptions that self and mutual inductance of the two windings are constant respect to θ.

The focus of this work is the proposal of a new control strategy on the current loops, so the first two equations of the model are discretized with forward Euler approximation:

$$\begin{aligned} i_{d,k+1} &= \left(1 - T_s \frac{R_s}{L_0}\right) i_{d,k} + i_{q,k}\omega_{e,k} T_s + \frac{T_s}{L_0}\hat{u}_{d,k} \\ i_{q,k+1} &= \left(1 - T_s \frac{R_s}{L_0}\right) i_{q,k} - i_{d,k}\omega_{e,k} T_s + \frac{T_s}{L_0}\hat{u}_{q,k} + \\ &\quad - \frac{k_M \omega_k}{L_0} T_s \end{aligned} \tag{2}$$

where T_s is the sampling time. The quantities $\hat{u}_{d,k}$ and $\hat{u}_{q,k}$ are the voltages that are physically applied to the motor. They are equal to $u^\star_{d,k} + \Delta u_{d,k}$ and $u^\star_{q,k} + \Delta u_{q,k}$, respectively $u^\star_{d,k}$ and $u^\star_{q,k}$ the optimal voltages computed by the control strategy and $\Delta u_{d,k}$, $\Delta u_{q,k}$ the components of the dead-time voltages. Figure 1 reports the dead-times voltages $\Delta u_{d,k}$ and $\Delta u_{q,k}$ in FW region during a load step. The dead-time voltages are taken into account in the following parameter extraction.

3 | Proposed Deadbeat Control

The proposed robust deadbeat control is reported in Figure 2. To save computational burden, the strategy uses deadbeat control (instead of M^{2}PC) for the reference voltages computation. The extraction of ΔL_0 and Δk_M is able to improve the accuracy of the motor model and the space vector modulation is adopted in place of the dwell times optimization based on minimizing the voltage error [17] or the current error [25] to save computational cost.

3.1 | Predicted Currents with Delay Compensation

The PWM delay compensation proposed in [32] is used to predict the currents at the instant $(k+1)$th as

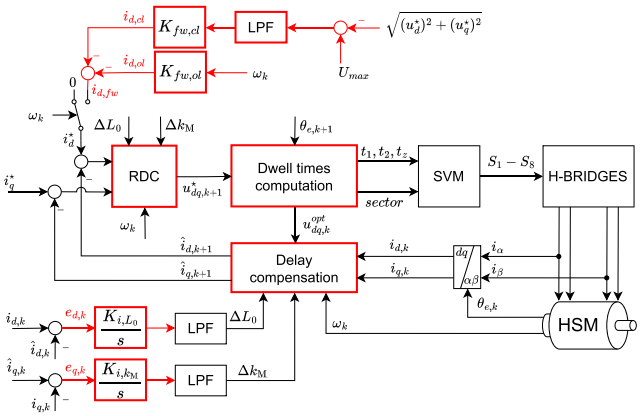


FIGURE 2 | Proposed robust deadbeat control (RDC) with parameter extraction, flux weakening and space vector modulation for two-phase machines. Red boxes are presented in detail in Section 3.

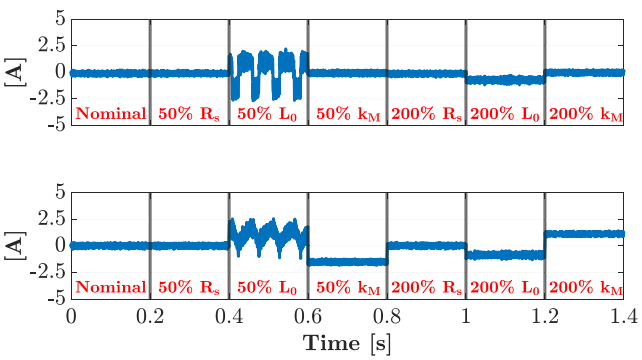


FIGURE 3 | Simulation results of $\hat{i}_{d,k} - i_{d,k}$ (top) and $\hat{i}_{q,k} - i_{q,k}$ (bottom) with classical deadbeat when the HSM parameters suddenly change in FW region.

$$\begin{aligned} \hat{i}_{d,k+1} &= \left(1 - T_s \frac{R_s}{\hat{L}_0}\right) i_{d,k} + i_{q,k}\omega_{e,k} T_s + \frac{T_s}{\hat{L}_0} u^\star_{d,k} \\ \hat{i}_{q,k+1} &= \left(1 - T_s \frac{R_s}{\hat{L}_0}\right) i_{q,k} - i_{d,k}\omega_{e,k} T_s + \frac{T_s}{\hat{L}_0} u^\star_{q,k} + \\ &\quad - \frac{\hat{k}_M \omega_k}{\hat{L}_0} T_s \end{aligned} \tag{3}$$

where $\hat{i}_{d,k+1}$ and $\hat{i}_{q,k+1}$ are the predicted stator currents, $i_{d,k}$ and $i_{q,k}$ are the measured currents. With respect to Equation (2) the quantities $\hat{L}_0$, $\hat{k}_M$, defined as the estimated values of L_0 and k_M, equal to $L_0 + \Delta L_0$ and $k_M + \Delta k_M$, respectively, are used to improve the model accuracy. Furthermore, the speed is considered as slowly varying, that is, $\omega_{e,k} \approx \omega_{e,k+1}$.

3.2 | ΔL_0 and Δk_M Extraction

The errors of $\hat{i}_{d,k} - i_{d,k}$ (where $\hat{i}_{d,k}$ is the predicted d-axis current at kth sampling instant) and $\hat{i}_{q,k} - i_{q,k}$ (where $\hat{i}_{q,k}$ is the predicted q-axis current at kth sampling instant) when the parameters suddenly augment/decrement using classical deadbeat (i.e., without ΔL_0 and Δk_M extraction) are displayed in Figure 3, highlighting the influence of the model parameters. In the simulation, the

17554543, 2026, 1, Downloaded from https://ietresearch.onlinelibrary.wiley.com/doi/10.1049/pel2.70318 by CochraneItalia, Wiley Online Library on [22/10/2026]. See the Terms and Conditions (https://onlinelibrary.wiley.com/terms-and-conditions) on Wiley Online Library for rules of use; OA articles are governed by the applicable Creative Commons License

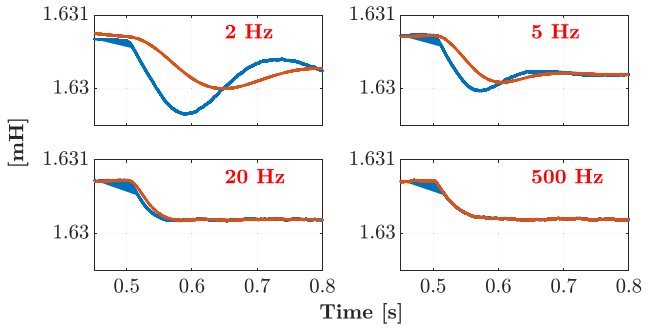


FIGURE 4 | Response to a load step from 0.5 to 1.5 Nm under constant speed of 140 rad/s with $T_{dt} = 1\,\mu$s for different values of the cut-off frequency f_{c,L_0}. The blue trace is the output of the integrator, whereas the orange trace is the output of the filter.

HSM runs in flux weakening region with a dead-time equal to zero. It is worth noting that when the resistance mismatch occurs, current errors are less influenced even in flux weakening region, whereas the stator inductance L_0 and the torque constant k_M exhibit a critical behaviour. So, it is important to extract precise information about L_0 and k_M.

The computation of the d-axis current prediction error $e_{d,k} = i_{d,k} - \hat{i}_{d,k}$ is here reported considering the voltage $\hat{u}_{d,k-1} = u^{\star}_{d,k-1} + \Delta u_{d,k-1}$ and the estimated quantities $\hat{R}_s$, $\hat{L}_0$ and $\hat{k}_M$ in Equation (2)

$$
\begin{aligned}
e_{d,k} &= T_s\left(\frac{\hat{R}_s}{\hat{L}_0} - \frac{R_s}{L_0}\right) i_{d,k-1} + T_s\left(\frac{\hat{u}_{d,k-1}}{L_0} - \frac{u^{\star}_{d,k-1}}{\hat{L}_0}\right) \\
\Delta L_0 &= \mathcal{Z}\left\{\frac{2\pi f_{c,L_0}}{s + 2\pi f_{c,L_0}}\right\}\mathcal{Z}\left\{\frac{K_{i,L_0}}{s}\right\} e_{d,k}
\end{aligned}
\tag{4}
$$

where s is the Laplace operator, $\mathcal{Z}$ is the Z-transform, f_{c,L_0} the cut-off frequency of the first order low pass filter (LPF), K_{i,L_0} the integral parameter and ΔL_0 the extracted parameter. The resistance error has no influence on current prediction error even in flux weakening region as demonstrated in Figure 3 and the torque constant is not a parameter of the equation, so the d-axis predicted current is mainly influenced by the inductance error and the dead-time voltage $\Delta u_{d,k}$ in $\hat{u}_{d,k-1}$. Changing the cutoff frequency of a low-pass filter directly shifts the boundary that separates the signals allowed to pass from those that are progressively attenuated. By reducing the cutoff frequency value, the filter becomes significantly more restrictive and cuts out a larger portion of the upper spectrum. In signal processing, it cleans the output of interference and sudden spikes, stabilizing the reading at the cost of making it less responsive (see for example Figure 4 with cutoff frequency of 2 Hz). Conversely, when this frequency is raised, the filter becomes more permissive and lets higher harmonic components through. In electronic sensors, it allows the capture of very rapid variations, though it exposes the system to a greater amount of high-frequency background noise as it happens for example in Figure 4 with cutoff frequency of 500 Hz.

The torque constant k_M is included in the q-axis current, considering the voltage $\hat{u}_{q,k-1} = u^{\star}_{q,k-1} + \Delta u_{q,k-1}$ in Equation (2) as well as the estimated electrical parameters. The expression of the error

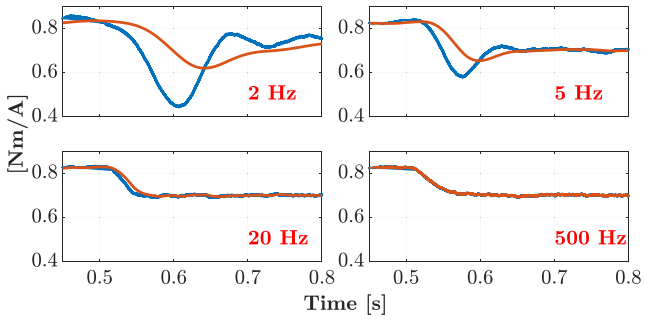


FIGURE 5 | Response to a load step from 0.5 to 1.5 Nm under constant speed of 140 rad/s with $T_{dt} = 1\,\mu$s for different values of the cut-off frequency f_{c,k_M}. The blue trace is the output of the integrator, whereas the orange trace is the output of the filter.

$e_{q,k} = \hat{i}_{q,k} - i_{q,k}$ is

$$
\begin{aligned}
e_{q,k} &= T_s\left(\frac{R_s}{L_0} - \frac{\hat{R}_s}{\hat{L}_0}\right) i_{q,k-1} + T_s\omega_k\left(\frac{k_M}{L_0} - \frac{\hat{k}_M}{\hat{L}_0}\right) + \\
&+ T_s\left(\frac{u^{\star}_{q,k-1}}{\hat{L}_0} - \frac{\hat{u}_{q,k-1}}{L_0}\right) \\
\Delta k_M &= \mathcal{Z}\left\{\frac{2\pi f_{c,k_M}}{s + 2\pi f_{c,k_M}}\right\}\mathcal{Z}\left\{\frac{K_{i,k_M}}{s}\right\} e_{q,k}
\end{aligned}
\tag{5}
$$

where f_{c,k_M} is the cut-off frequency of the first order LPF, K_{i,k_M} is the integral parameter. The stator resistance mismatch ΔR_s has low influence as shown in Figure 3 and it can be neglected. Considering the stator inductance already corrected by Equation (4), the expression of $e_{q,k}$ is simplified as

$$
e_{q,k} = -T_s\omega_k\frac{\hat{k}_M - k_M}{L_0} - T_s\frac{\hat{u}_{q,k-1} - u^{\star}_{q,k-1}}{L_0} \tag{6}
$$

The same observations made for Figure 4 also hold true for Figure 5.

3.2.1 | Low Speed Issues Under No-Load Condition

Although the primary focus of this manuscript is on the flux weakening operation of a machine with a high number of pole pairs, the subsequent section will discuss its operation at very low speeds under no-load conditions. When the machine operates at very low speeds under no-load conditions, the extraction of the parameter ΔL_0 induces an increase in the ripple of both the dq currents and, consequently, a distortion on the output currents. This behaviour stems from the fact that at small duty cycle values, the dq voltages are inherently low, which hinders the accurate extraction of the inductance. As a countermeasure, it is recommended to enable the extraction of ΔL_0 only at higher rotational speeds.

Figure 6 shows the no-load dq currents with and without ΔL_0 extraction, while Figure 7 reports the output current under a load torque of 2 Nm. Both tests are conducted at a very low speed of 2 rad/s and confirm the previously discussed considerations.

17554543, 2026, 1, Downloaded from https://ietresearch.onlinelibrary.wiley.com/doi/10.1049/pel2.70318 by Cochraneltalia, Wiley Online Library on [22/10/2026]. See the Terms and Conditions (https://onlinelibrary.wiley.com/terms-and-conditions) on Wiley Online Library for rules of use; OA articles are governed by the applicable Creative Commons License

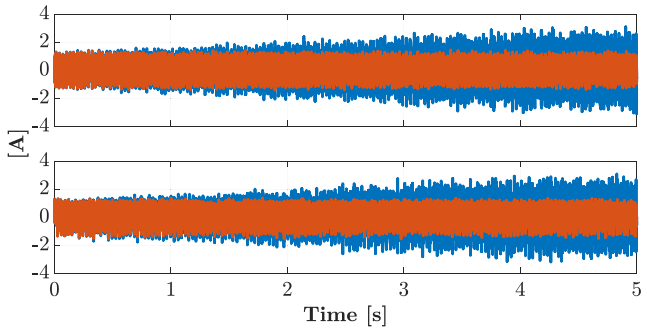


FIGURE 6 | Response at no-load condition under constant speed of 2 rad/s with $T_{dt} = 1$ µs. The blue traces are the dq currents using the extraction of ΔL_0, whereas the orange traces are the dq currents without the extraction of ΔL_0.

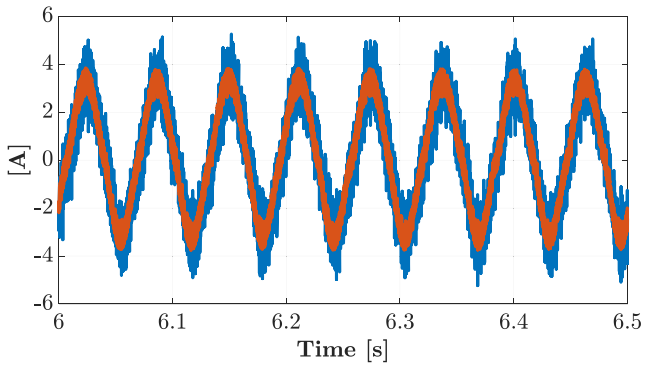


FIGURE 7 | Response with a load torque of 2 Nm under constant speed of 2 rad/s with $T_{dt} = 1$ µs. The blue trace is the output current i_α using the extraction of ΔL_0, whereas the orange trace is the output current i_α without the extraction of ΔL_0.

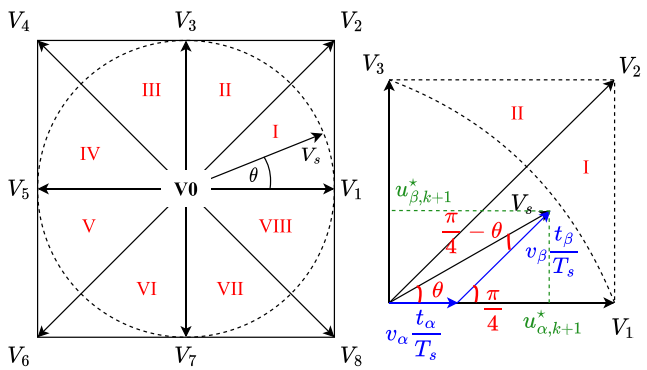


FIGURE 8 | Details of the space vector modulation used for two phase machines. The dashed red lines are an example of $u^\star_{\alpha,k+1}$ and $u^\star_{\beta,k+1}$.

3.3 | Robust Deadbeat Control

The choice of deadbeat predictive current control allow saving computational cost. In fact, with M^{2}PC control, the selection of the optimal sector is done using the full active vectors located on the square of the space vector modulation diagram (see Figure 8). This choice increase the computational burden of the strategy because two active vectors at a time needs to be predicted. Therefore, the use of the full active vector in the prediction can bring to errors on the selection of the optimal sector.

The optimal voltages $u^\star_{d,k+1}$, $u^\star_{q,k+1}$ are computed to nullify the current errors after two sampling periods. It is worth noting that only one calculation is required, avoiding the enumeration of every active vector. To compensate the delay, Equation (3) is adopted, and then $\hat{i}_{d,k+1}, \hat{i}_{q,k+1}$ are used to compute the new voltage vectors, applied at the next sampling instant. The reference voltages are

$$\begin{aligned} u^\star_{d,k+1} &= \frac{\hat{L}_0}{T_s}\left(i^\star_{d,k} - \hat{i}_{d,k+1}\right) + R_s\hat{i}_{d,k+1} + \\ &\quad - \omega_{e,k}\hat{i}_{q,k+1}\hat{L}_0 \\ u^\star_{q,k+1} &= \frac{\hat{L}_0}{T_s}\left(i^\star_{q,k} - \hat{i}_{q,k+1}\right) + R_s\hat{i}_{q,k+1} + \omega_k\hat{k}_M + \\ &\quad + \omega_{e,k}\hat{i}_{d,k+1}\hat{L}_0 \end{aligned} \tag{7}$$

The dq reference voltages are simply computed following the well-known deadbeat principle with the use of $\hat{L}_0$ and $\hat{k}_M$ in place of the nominal parameters.

3.4 | Flux Weakening Control

To work in flux weakening region, a simple control strategy based on the measured speed ω_k is adopted. The classical FW control based on output voltage regulation is avoided due the well-known problems of large sixth harmonic current, windup and even instability problems [33]. The flux weakening control is implemented by adding an open-loop component and a closed-loop component. The open-loop component named $i_{d,\text{ol}}$ is considered equal to $K_{\text{fw, ol}}(\omega - \omega_N)/(\omega_{\max} - \omega_N)$, where $K_{\text{fw, ol}}$ is a proportional gain, ω_N is the base speed, and $\omega_{\max}$ is the maximum speed of the HSM. The closed-loop component is obtained by closing another loop on the error between the available voltage $U_{\max}$ and the demanded voltage module $\sqrt{u^{\star 2}_d + u^{\star 2}_q}$. This error is filtered by a LPF and regulated with a proportional gain $K_{\text{fw, cl}}$. The result is the closed-loop current called $i_{d,\text{cl}}$. Summarizing, the flux weakening current $i_{d,\text{fw}}$ equal to $-i_{d,\text{cl}} - i_{d,\text{ol}}$ is

$$\begin{aligned} i_{d,\text{fw}} &= -K_{\text{fw, ol}} \cdot \left(\frac{\omega - \omega_N}{\omega_{\max} - \omega_N}\right) + \\ &\quad - K_{\text{fw, cl}} \cdot \text{LPF}\left(U_{\max} - \sqrt{u^{\star 2}_d + u^{\star 2}_q}\right) \end{aligned} \tag{8}$$

The current reference $i^\star_d$ is computed when the nominal speed ω_N in Table 2 is overcome without the use of the LPF (see [24] for more details), resulting in

$$i^\star_d = \begin{cases} 0, & \text{for } \omega \le \omega_N \\ i_{d,\text{fw}}, & \text{for } \omega > \omega_N \end{cases} \tag{9}$$

where K_{fw} is a proportional gain and $\omega_{\max}$ is the maximum speed of the drive. The minimum allowed $i^\star_d$ is equal to −5 A.

17554543, 2026, 1, Downloaded from https://ietresearch.onlinelibrary.wiley.com/doi/10.1049/pel2.70318 by CochraneItalia, Wiley Online Library on [22/10/2026]. See the Terms and Conditions (https://onlinelibrary.wiley.com/terms-and-conditions) on Wiley Online Library for rules of use; OA articles are governed by the applicable Creative Commons License

TABLE 2 | HSM parameters.

Parameter	Symbol	Value	Unit
DC bus voltage	V_{DC}	70	V
Nominal phase current	I_N	10	A_{pk}
Poles pairs/rotor teeth	N_r	50	—
Stator resistance	R_s	0.187	Ω
Stator inductance	L_0	1.63	mH
Torque constant	k_M	0.645	Nm/A
Nominal torque	T_L	5.2	Nm
Nominal speed	ω_N	100	rad/s

3.5 | Space Vector Modulation

In the middle-high speed range, the PWM delay (due to sampling time T_s) can have a significant impact on the rotor position, so to maximize the performance for all the controls, the electrical angle at $(k+1)$th sampling instant used for dq to $\alpha\beta$ transformation is predicted as [3]

$$\theta_{e,k+1} = \theta_{e,k} + 1.5T_s\omega_{e,k} \tag{10}$$

The voltages in the fixed frame are computed with dq to $\alpha\beta$ transformation as

$$\begin{bmatrix} u^\star_{\alpha,k+1} \\ u^\star_{\beta,k+1} \end{bmatrix} = \begin{bmatrix} \cos(\theta_{e,k+1}) & -\sin(\theta_{e,k+1}) \\ \sin(\theta_{e,k+1}) & \cos(\theta_{e,k+1}) \end{bmatrix} \begin{bmatrix} u^\star_{d,k+1} \\ u^\star_{q,k+1} \end{bmatrix} \tag{11}$$

With the predicted reference voltages in the fixed reference frame, the quadrant is extracted from the signs of $u^\star_{\alpha,k+1}$ and $u^\star_{\beta,k+1}$, while the sector is extracted from trigonometric computations following the SVM principle for two phase machines displayed in Figure 8. Once the sector is selected, the space vector modulation for two-phase machines is used. SVM for two-phase motors is reported in stationary reference frame (α, β) in Figure 8. With this power electronics, there are 8 active vectors labelled from V_1 to V_8 and 4 zero vectors labelled with V_0 in the origin. The predicted reference voltage vector V_s and the angle θ are identified as

$$\begin{aligned} V_s &= \sqrt{(u^\star_{\alpha,k+1})^2 + (u^\star_{\beta,k+1})^2} \\ \theta &= \text{atan}(u^\star_{\beta,k+1}/u^\star_{\alpha,k+1}) \end{aligned} \tag{12}$$

Using this information, two active vectors v_α and v_β and one zero vector are used to synthesize the reference voltage vector V_s. The optimal voltages $u^\star_{d,k}$ and $u^\star_{q,k}$ used for the delay compensation in Equation (3) are computed from $u^\star_{d,k+1}$ and $u^\star_{q,k+1}$ applying a delay of one sample.

4 | Simulations Results

The modelling and simulation of the control structure drive system is carried out using PLECS environment. A commercial stepper motor (AM34SS3DGA-N) with 50 poles pairs/rotor teeth employing an incremental encoder with 20,000 counts/rev is used for simulation/experimental, see Table 2 for nameplate data. In order to take into consideration the finite resolution of analogue-to-digital converters (ADCs) and digital pulse width modulation (PWM) peripherals, the control schemes have been discretized (T_s = 50 µs), while measured currents and applied voltages have been quantized to 16 bits resolution. The switching frequency f_{sw} is set to 20 kHz and coincides with the sampling frequency f_s.

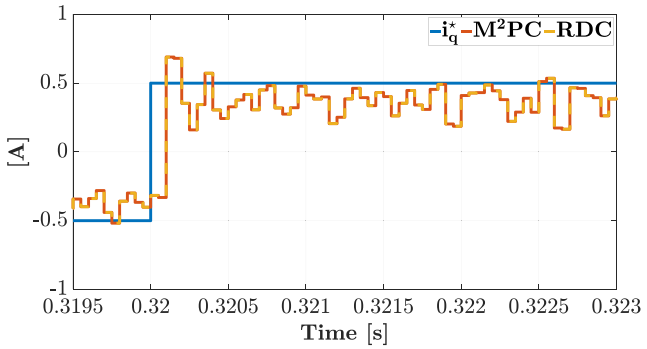


FIGURE 9 | Step response with amplitude of 0.5 A and frequency of 100 Hz.

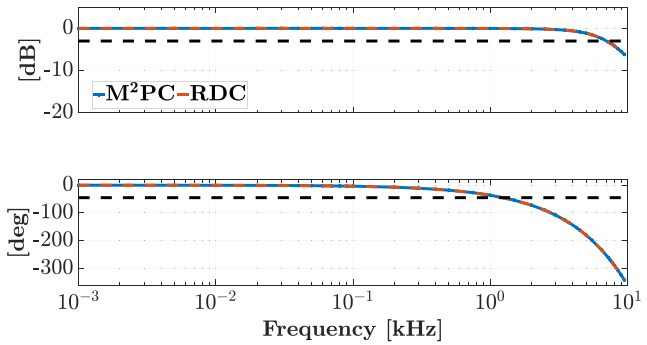


FIGURE 10 | Closed loop Bode diagram of $i_q/i_q^\star$. Black dashed lines are the attenuation of −3 dB (top) and the phase delay of 45° (bottom).

The following control strategies are considered:

- classical M²PC control;
- proposed robust deadbeat control with parameter extraction and SVM (named as RDC in the following).

The step response of the control strategies is computed at standstill, imposing a step reference with small amplitude of 0.5 A and frequency of 100 Hz. Same results are obtained with M²PC and RDC that have a rise time of two samples.

Figure 10 reports the closed loop Bode diagrams of $i_q^\star/i_q$ of the control strategies, putting in evidence that M²PC and RDC have the same the bandwidth, both considering the attenuation of −3 dB on the magnitude and the delay of 45° on the phase. The diagram is in accordance with the results of [3] in case of sinusoidal references.

The behaviour of the control strategies in the low speed region is assessed in Figure 11. The HSM runs from 20 to 60 rad/s with a constant load torque of 2 Nm considering a dead-time T_{dt} of 1 µs,

17554543, 2026, 1, Downloaded from https://ietresearch.onlinelibrary.wiley.com/doi/10.1049/pel2.70318 by CochraneItalia, Wiley Online Library on [22/10/2026]. See the Terms and Conditions (https://onlinelibrary.wiley.com/terms-and-conditions) on Wiley Online Library for rules of use; OA articles are governed by the applicable Creative Commons License

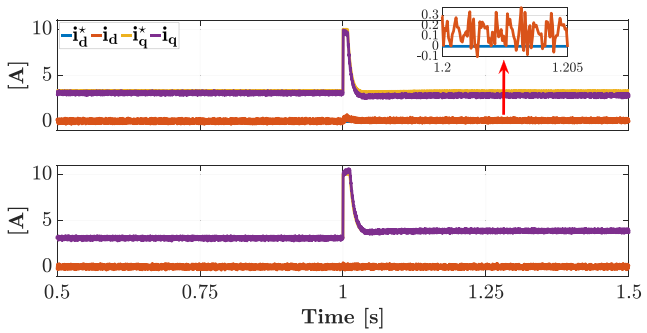


FIGURE 11 | Response to a step between 20 and 60 rad/s under constant load torque of 2 Nm with M²PC (top) and RDC (bottom) with dead-time of 1 μs, $\hat{L}_0 = 1.2\,L_0$ and $\hat{k}_M = 1.1 k_M$.

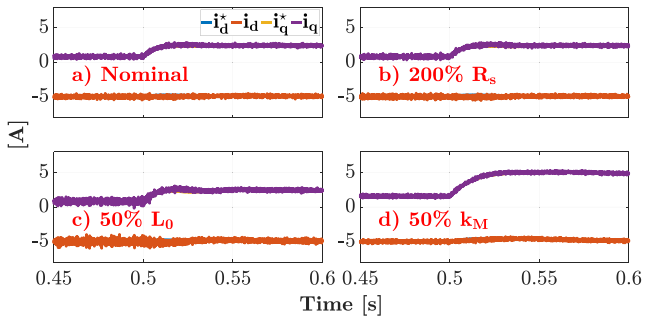


FIGURE 12 | Simulation with parameters mismatch using the proposed control: response to a load step from 0.5 to 1.5 Nm under constant speed of 140 rad/s with $T_{dt} = 1$ μs. (a) Nominal parameters; (b) R_s of the HSM is doubled; (c) L_0 of the HSM is halved; (d) k_M of the HSM is halved.

the stator inductance of the motor equal to 1.2 times the nominal one and the torque constant equal to 1.1 times the nominal one. It can be seen that the classical M²PC has a visible steady-state error on the q axis, while the error on the d axis is smaller and reported in the zoomed plot. Furthermore, the proposed RDC has the ability of control both currents without errors during the transient and in steady-state.

The effect of the parameter variation in flux weakening region is studied for the previous controls. In practical applications, the stator inductance L_0 is dependent on magnetic saturation effects and decreases with the current, whereas the stator resistance R_s increases with temperature. Furthermore, the torque constant k_M decreases during overload operations or as the temperature increases; hence the produced torque becomes smaller, making its estimation necessary to monitor demagnetization, so these three situations are studied in the following. Electrical parameters of the hybrid stepper motor drive are modified one at a time, keeping the others at the nominal value.

Imposing a speed reference of 140 rad/s, using RDC in Figure 12, the response of the system is the same in case of nominal parameters and errors on one parameter at a time.

Using the proposed RDC, Figures 13 and 14 show the low pass filter output in case of ΔL_0 and Δk_M extraction with different electrical parameters errors and different dead-times T_{dt}. Without dead-time T_{dt} in Figure 13 values of $\hat{L}_0$ approach to the correct

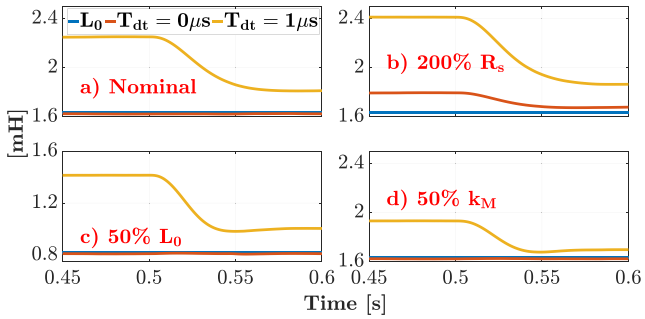


FIGURE 13 | Simulation with ΔL_0 extraction with electrical parameters errors: response to a load step from 0.5 Nm to 1.5 Nm under constant speed of 140 rad/s with different dead-times. (a) Nominal parameters; (b) R_s of the HSM is doubled; (c) L_0 of the HSM is halved; (d) k_M of the HSM is halved.

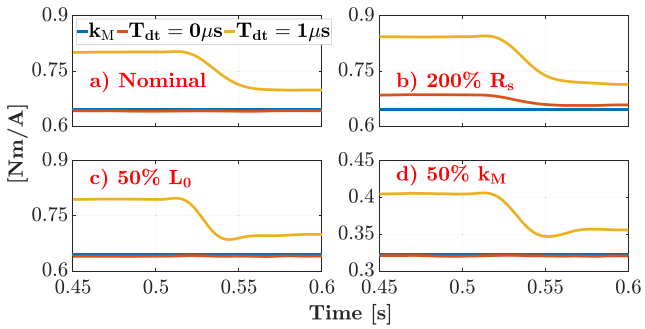


FIGURE 14 | Simulation with Δk_M extraction with electrical parameters errors: response to a load step from 0.5 to 1.5 Nm under constant speed of 140 rad/s with different dead-times. (a) Nominal parameters; (b) R_s of the HSM is doubled; (c) L_0 of the HSM is halved; (d) k_M of the HSM is halved.

value in case of nominal values and with errors on the knowledge of L_0 and k_M. The error on R_s has negligible influence, even in FW region: the error on extraction of $\hat{L}_0$ is under 0.2 mH. Inserting a dead-time T_{dt} equal to 1 μs, $\hat{L}_0$ works to nullify the error and include the dead-time voltage in its extraction in any scenario, even in case of nominal parameters, in accordance with the analysis in Section 3.2. Results put in evidence that the major source of error is due to dead-time.

Figure 14 shows the extraction of $\hat{k}_M$. The strategy has a correct estimation of the torque constant with nominal values and errors on L_0 and k_M if the dead-time is omitted from the model. Even in this case, the error on R_s has a negligible impact: in fact, the error on the extraction of k_M is under 0.05 Nm/A. With the dead-time T_{dt} equal to 1 μs, it can be seen from Figure 14 that the calculation of $\hat{k}_M$ is influenced by the presence of the dead-time. It should be noted that despite the error in the extraction of ΔL_0 and Δk_M when R_s is wrong, the dq current is properly regulated as shown in Figure 12.

The controls are tested with a speed reference $\omega^\star$ of 250 rad/s using nominal electrical parameters and a dead-time T_{dt} equal to 1 μs. From Figure 15, it can be seen that the proposed RDC is able to reach the speed reference. M²PC cannot reach this operating condition. Usually the cost function is based on the square of the

17554543, 2026, 1, Downloaded from https://ietresearch.onlinelibrary.wiley.com/doi/10.1049/pel2.70318 by CochraneItalia, Wiley Online Library on [22/10/2026]. See the Terms and Conditions (https://onlinelibrary.wiley.com/terms-and-conditions) on Wiley Online Library for rules of use; OA articles are governed by the applicable Creative Commons License

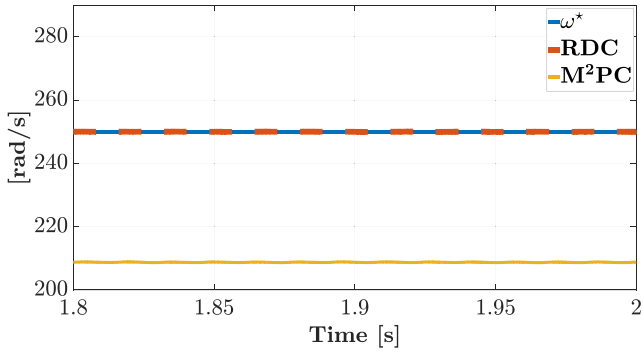


FIGURE 15 | Steady-state speeds with a speed reference $\omega^\star$ of 250 rad/s, load torque of 0.5 Nm and T_{dt} of 1 µs.

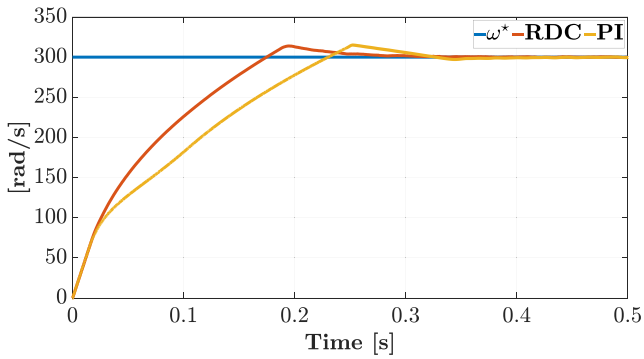


FIGURE 16 | Comparison between RDC and PI with a speed reference $\omega^\star$ of 300 rad/s, load torque of 0.1 Nm and T_{dt} of 1 µs.

current errors on both dq axis (see for example [3, 18, 34]) with $i_d^\star$ equal to 0 A, but in this situation, in FW region, both $i_d^\star$ and $i_q^\star$ are modified by the control.

Since M^{2}PC does not reach the reference at the required speed of 300 rad/s (the electrical frequency is ≈2400 Hz), the PI control is taken into consideration. From Figure 16 it can be seen that the overshoot is comparable, but the proposed control is able to reach the speed reference with lower rise time and lower settling time with respect to the traditional PI control confirming the advantages of deadbeat-based controls in case of low carrier ratio [30].

5 | Experimental Results

The control schemes have finally been tested by experiments. The controllers are implemented in their discrete version on a commercial STM32H743ZI digital signal processor (DSP) controller. The DSP is used to implement the proposed controls, as well as to generate the PWM signals and to acquire the two motor phase currents.

The HSM is installed on the test bench shown in Figure 17, which also includes a torquemeter and a brushless machine as a brake. The HSM nameplate data are shown in Table 2. The IRS2184S half-bridge gate driver with a dead-time T_{dt} of 400 ns is used on the power board.

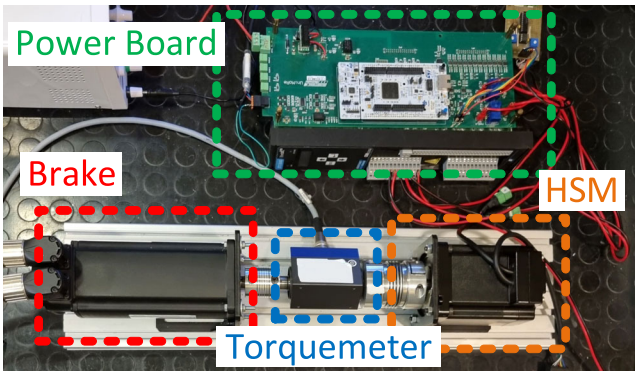
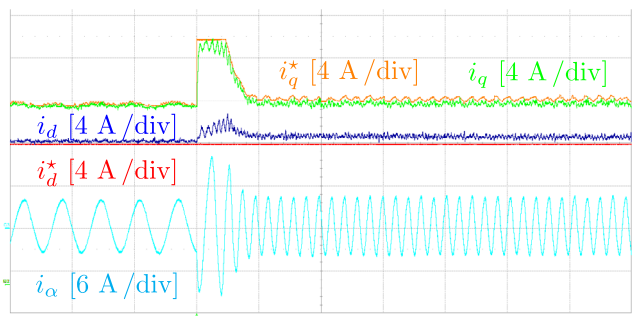
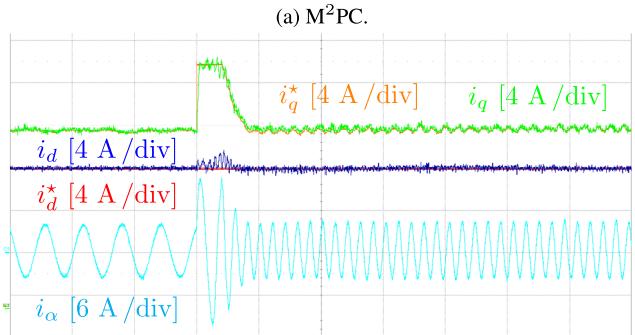


FIGURE 17 | Test bench with HSM, brake, torquemeter and power board.



(a) M^{2}PC.



(b) RDC.

FIGURE 18 | Test 1: response to a step between 20 and 60 rad/s under constant load torque of 2 Nm. The time division is 10 ms/div.

5.1 | Test 1: Speed Step with Constant Torque in Low Speed Region

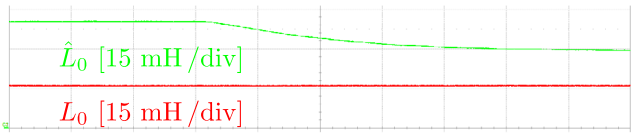
A speed-loop analysis has been carried out. The loop is closed on a PI regulator. Experimental tests have been carried out imposing a constant load torque of 2 Nm with a variable speed reference from 20 to 60 rad/s. M^{2}PC in Figure 18a exhibits steady-state errors when the rotor moves due to incorrect values of $\hat{L}_0$ and $\hat{k}_{\mathrm{M}}$ used in the control. From Figure 18b it can be seen that the use of RDC improves the performance of M^{2}PC in low speed region determining lower power losses, vibration and acoustic noise.

Table 3 summarizes the results in terms of THD for the test of Figure 18. It is worth noting that M^{2}PC and RDC have comparable THDs in this scenario.

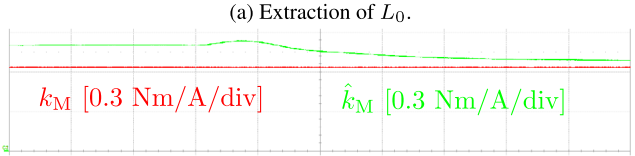
17554543, 2026, 1, Downloaded from https://ietresearch.onlinelibrary.wiley.com/doi/10.1049/pel2.70318 by CochraneItalia, Wiley Online Library on [22/10/2026]. See the Terms and Conditions (https://onlinelibrary.wiley.com/terms-and-conditions) on Wiley Online Library for rules of use; OA articles are governed by the applicable Creative Commons License

TABLE 3 | Phase current THD [%] comparison with Test 1.

	$\omega^\star = 20$ rad/s	$\omega^\star = 60$ rad/s
M²PC	4.12	6.22
RDC	3.99	6.13



(a) Extraction of L_0.



(b) Extraction of k_M.

FIGURE 19 | Test 2: extraction of L_0 (top) and k_M (bottom) with $\omega^\star$ of 140 rad/s and a load step from 0 to 1 Nm. Red: nominal parameter, green: extracted parameter. The time division is 50 ms/div.

TABLE 4 | Phase current THD [%] comparison with Test 3 at 160 rad/s.

	$T_L = 0$ Nm	$T_L = 1$ Nm
M²PC	6.36	6.21
RDC	6.84	5.92

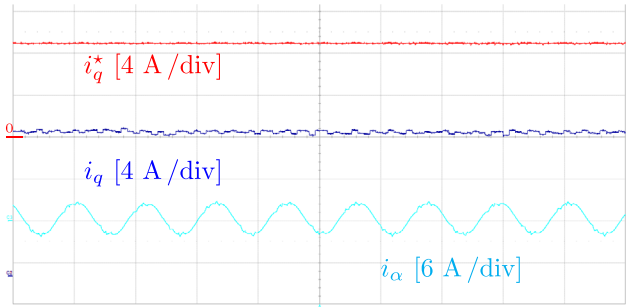
5.2 | Test 2: ΔL_0 and Δk_M Extraction in Flux Weakening Region

The strategies for the extraction of ΔL_0 and Δk_M exposed in Section 3.2 are tested in this section in flux weakening region. In Figure 19 a speed reference of 140 rad/s is imposed with a load step from 0 to 1 Nm. It can be seen that for both parameters the behaviour is in accordance with the one of Section 4 in Figures 13 and 14. When the load step is applied both $\hat{L}_0$ and $\hat{k}_M$ tend to converge to the nominal value despite the error given by dead-time.

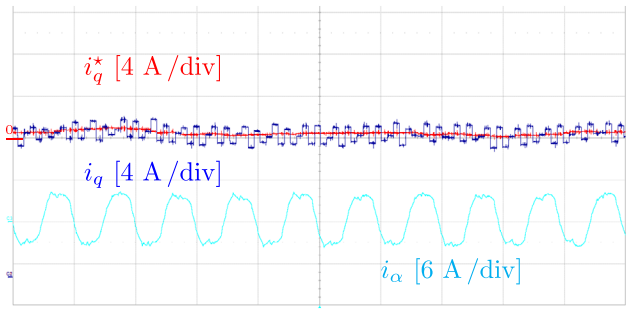
5.3 | Test 3: Flux Weakening Region

The HSM is tested in FW region with different speeds and different loads. The results with a speed reference of 160 rad/s and different loads (in this case, at no-load condition and with 1 Nm of load torque) are reported in Table 4: in this situation, the THDs are comparable for both control strategies. This confirms the fact that the traditional M²PC and the proposed RDC have similar behaviour when they are able to reach the same speed/torque operating conditions. The proposed strategy demonstrates superior performance in the deep flux weakening region.

In fact, increasing the speed reference the behaviour of M²PC is reported in Figure 20a putting in evidence that in FW region the control is not able to reach the desired speed/torque operating condition. In Figure 20a the measured speed is 221 rad/s. The proposed RDC is able to reach the speed reference in Figure 20b.

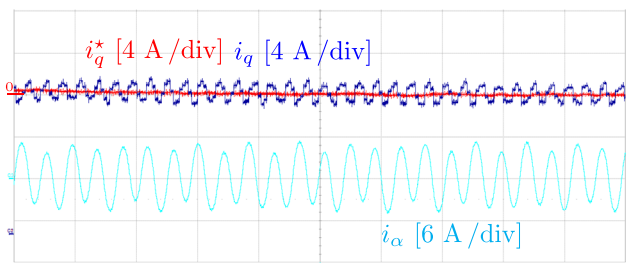


(a) M²PC.

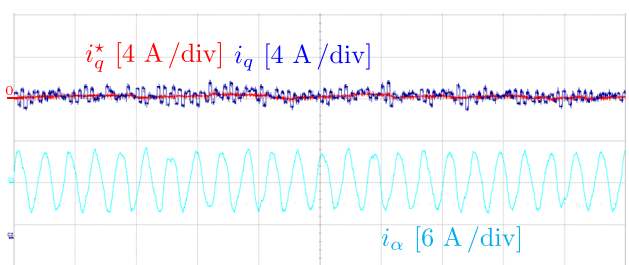


(b) RDC.

FIGURE 20 | Test 3: steady-state currents with a speed reference of 250 rad/s at no load. The time division is 500 µs/div.



(a) PI.



(b) RDC.

FIGURE 21 | Test 4: steady-state currents with a speed reference of 300 rad/s at no load. The time division is 1 ms/div.

5.4 | Test 4: Comparison with PI Under Low Carrier Ratio

One last test in case of low carrier ratio is performed comparing traditional PI control and RDC in Figure 21. It can be seen that PI control has more oscillations on the i_q current (and consequently on the output currents) respect to RDC in Figure 21b. The fast Fourier transform (FFT) for the test of Figure 21 is reported in

17554543, 2026, 1, Downloaded from https://ietresearch.onlinelibrary.wiley.com/doi/10.1049/pel2.70318 by CochraneItalia, Wiley Online Library on [22/10/2026]. See the Terms and Conditions (https://onlinelibrary.wiley.com/terms-and-conditions) on Wiley Online Library for rules of use; OA articles are governed by the applicable Creative Commons License

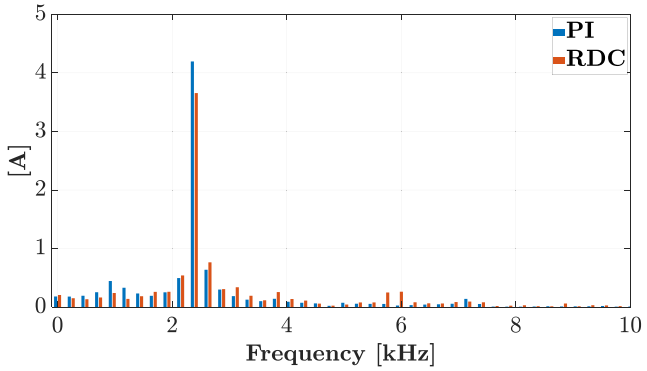


FIGURE 22 | Test 4: fast Fourier transform of the output current i_α.

TABLE 5 | Computational cost of implemented strategies.

	M²PC	RDC
Time [μs]	18.19	9.49

Figure 22 showing that the proposed RDC has lower root mean square (RMS) on the fundamental frequency with respect to classical PI. Furthermore, greater presence of subharmonics can be observed in PI with respect to RDC. It should be noted that the iron loss resistance R_i [35–37] is not modelled in the electrical system, despite this omission, the proposed strategy based on the motor model is able to maintain the control of the drive.

5.5 | Computational Cost

The computational cost of the strategies is compared when the control is closed on the speed loop, taking into consideration only the execution times of the current control loops. The algorithms run on an internal clock of 480 MHz and the results are summarized in Table 5. Time measures confirm the advantage of RDC in terms of computational cost with respect to M²PC.

6 | Conclusions

This paper analyses the performance of a novel RDC strategy, evaluating its step response and bandwidth in current loops at standstill. The behaviour of the RDC in the flux weakening region at higher speeds is also investigated. A comparison is made between the proposed RDC strategy and a high-performance M²PC strategy. The key findings are summarized as follows:

- the impact of dead-time is considered during the extraction of the electrical parameters L_0 and k_M, demonstrating that the estimation is influenced by this parameter;
- at standstill, the step response for M²PC and RDC is the same, as confirmed by the closed-loop Bode diagram, which indicates similar bandwidths for both predictive control methods;
- RDC improves performance compared to M²PC in the low-speed region, specifically in terms of steady-state errors;
- in the FW region, at higher speeds, the proposed RDC achieves a higher maximum speed compared to M²PC. In particular, M²PC is limited to a maximum speed of 221 rad/s, whereas RDC extends the operational range up to 300 rad/s, representing a 35.7% performance improvement;
- RDC requires fewer computational resources than M²PC, with a reduction of 47.83%;
- RDC, which is a deadbeat-based control, confirms the ability to maintain the control on the dq currents in case of low carrier ratio with respect to traditional PI.

Future research will focus on developing a more accurate electrical model to better represent the machine's behaviour in the high-speed region, particularly considering the dominant effect of iron losses in high pole count machines.

Author Contributions

Emilio Carfagna: conceptualization, methodology, software, validation, investigation, data curation, writing – original draft preparation, writing – review and editing; **Fabio Bernardi:** conceptualization, methodology, software, writing – review and editing; **Giovanni Migliazza:** software, validation, investigation, writing – original draft preparation, writing – review and editing; **Emilio Lorenzani:** funding acquisition, supervision, writing – original draft preparation, writing – review and editing. All authors have read and agreed to the published version of the manuscript.

Acknowledgments

Open access publishing facilitated by Università degli Studi di Modena e Reggio Emilia, as part of the Wiley - CRUI-CARE agreement.

Funding

This work was supported by the National Recovery and Resilience Plan (NRRP), Mission 04 Component 2 Investment 1.5 – NextGenerationEU (Grant No. 0001052).

Conflicts of Interest

The authors declare no conflicts of interest.

Data Availability Statement

The authors elect to not share data.

References

1. N. Taran, V. Rallabandi, G. Heins, and D. M. Ionel, "Systematically Exploring the Effects of Pole Count on the Performance and Cost Limits of Ultrahigh Efficiency Fractional HP Axial Flux PM Machines," *IEEE Transactions on Industry Applications* 56, no. 1 (2020): 117–127.

2. S.-U. Chung, S.-H. Moon, D.-J. Kim, and J.-M. Kim, "Development of a 20-Pole-24-Slot SPMSM with Consequent Pole Rotor for In-Wheel Direct Drive," *IEEE Transactions on Industrial Electronics* 63, no. 1 (2016): 302–309.

3. F. Bernardi, E. Carfagna, G. Migliazza, G. Buticchi, F. Immovilli, and E. Lorenzani, "Performance Analysis of Current Control Strategies for Hybrid Stepper Motors," *IEEE Open Journal of the Industrial Electronics Society* 3 (2022): 460–472.

4. A. M. Diab, F. Guo, S. S. Yeoh, S. Bozhko, C. Gerada, and M. Galea, "Comparative Stability Analysis of Synchronous Reference Frame

17554543, 2026, 1, Downloaded from https://ietresearch.onlinelibrary.wiley.com/doi/10.1049/pel2.70318 by CochraneItalia, Wiley Online Library on [22/10/2026]. See the Terms and Conditions (https://onlinelibrary.wiley.com/terms-and-conditions) on Wiley Online Library for rules of use; OA articles are governed by the applicable Creative Commons License

Current Controllers Operated at High Fundamental Frequency," *IEEE Transactions on Transportation Electrification* 9, no. 2 (2023): 2115–2128.

5. M. Sun, Y. Yao, X. Zhao, et al., "Precise Aspiration and Positioning Control Based on Dynamic Model Inside and Outside the Micropipette," *IEEE Transactions on Automation Science and Engineering* 20, no. 1 (2023): 385–393.

6. Y. Zhang, M. Q.-H. Meng, and L. Liu, "Design and Control of a Compact Electromagnetically Driven Laser Scanner for Robotic-Assisted Endoscopic Microsurgeries," *IEEE Transactions on Automation Science and Engineering* 21, no. 4 (2024): 5997–6010.

7. Y.-L. Huang, C.-H. Liang, B.-H. Chen, and C.-C. Lan, "Torque-Sensorless Control of Stepper Motors for Low-Cost Compliant Motion Generation," *IEEE Access* 9 (2021): 94495–94504.

8. N. Matsui, M. Nakamura, and T. Kosaka, "Instantaneous Torque Analysis of Hybrid Stepping Motor," *IEEE Transactions on Industry Applications* 32, no. 5 (1996): 1176–1182.

9. A. Arias, J. Caum, E. Ibarra, and R. Griñó, "Reducing the Cogging Torque Effects in Hybrid Stepper Machines by Means of Resonant Controllers," *IEEE Transactions on Industrial Electronics* 66, no. 4 (2019): 2603–2612.

10. A. EL-Refaie and T. Jahns, "Optimal Flux Weakening in Surface PM Machines Using Fractional-Slot Concentrated Windings," *IEEE Transactions on Industry Applications* 41, no. 3 (2005): 790–800.

11. H. Liu, Z. Q. Zhu, E. Mohamed, Y. Fu, and X. Qi, "Flux-Weakening Control of Nonsalient Pole PMSM Having Large Winding Inductance, Accounting for Resistive Voltage Drop and Inverter Nonlinearities," *IEEE Transactions on Power Electronics* 27, no. 2 (2012): 942–952.

12. E. Zerdali, M. Rivera, and P. Wheeler, "A Review on Weighting Factor Design of Finite Control Set Model Predictive Control Strategies for AC Electric Drives," *IEEE Transactions on Power Electronics* 39, no. 8 (2024): 9967–9981.

13. D. Xu, Y. Yao, F. Peng, and Y. Huang, "Simplified Continuous-Control-Set Model Predictive Control for LCL-Equipped High-Speed PMSM with High Dynamic Performance," *IEEE Transactions on Industrial Electronics* 72, no. 5 (2025): 4661–4670.

14. Z. Sun, Y. Deng, J. Wang, and H. Li, "Robust Three-Voltage-Vector-Based Model-Free Predictive Current Control for Permanent Magnet Synchronous Motor with Ultra-Local Model," *IET Power Electronics* 16, no. 16 (2023): 2739–2753.

15. C. Xia, M. Wang, Z. Song, and T. Liu, "Robust Model Predictive Current Control of Three-Phase Voltage Source PWM Rectifier with Online Disturbance Observation," *IEEE Transactions on Industrial Informatics* 8, no. 3 (2012): 459–471.

16. D. Yu, C. Zhang, Q. Guo, and M. Zhou, "Low Complexity Duty Cycle Modulation Model Predictive Current Control of Permanent Magnet Synchronous Motor," *IET Power Electronics* 16, no. 3 (2023): 413–422.

17. A. Aboelhassan, S. Wang, Y. Mikhaylov, G. Buticchi, M. Galea, and S. Bozhko, "Discontinuous Modulated Model Predictive Control for Low Inductance High-Speed Electric Drive Applications," *IEEE Transactions on Industrial Electronics* 71, no. 7 (2024): 6689–6698.

18. F. Morel, X. Lin-Shi, J.-M. Retif, B. Allard, and C. Buttay, "A Comparative Study of Predictive Current Control Schemes for a Permanent-Magnet Synchronous Machine Drive," *IEEE Transactions on Industrial Electronics* 56, no. 7 (2009): 2715–2728.

19. Q. Xu and S. Fang, "Robust Deadbeat Predictive Current Sensorless Control for Permanent Magnet Synchronous Motor," *IEEE Transactions on Power Electronics* 39, no. 9 (2024): 11441–11454.

20. L. Wang, S. Zhang, C. Zhang, and Y. Zhou, "An Improved Deadbeat Predictive Current Control Based on Parameter Identification for PMSM," *IEEE Transactions on Transportation Electrification* 10, no. 2 (2024): 2740–2753.

21. M. Tang, A. Gaeta, A. Formentini, K. Ohyama, P. Zanchetta, and G. Asher, "Enhanced DBCC for High-Speed Permanent Magnet Synchronous Motor Drives," *IET Power Electronics* 9, no. 15 (2016): 2880–2890.

22. A. Aboelhassan, S. Wang, G. Buticchi, V. Varvolik, M. Galea, and S. Bozhko, "Modulated Model Predictive Speed Controller for PMSM Drives Employing Voltage-Based Cost Function," *IEEE Open Journal of the Industrial Electronics Society* 5 (2024): 122–131.

23. S. Dai, J. Wang, Z. Sun, and E. Chong, "Deadbeat Predictive Current Control for High-Speed Permanent Magnet Synchronous Machine Drives with Low Switching-to-Fundamental Frequency Ratios," *IEEE Transactions on Industrial Electronics* 69, no. 5 (2022): 4510–4521.

24. E. Carfagna, G. Migliazza, M. Medici, and E. Lorenzani, "Performance Comparison Between Microstepping and Field-Oriented Control for Hybrid Stepper Motors," *Energies* 18, no. 3 (2025): 553.

25. Q. Dong, B. Wang, L. Xia, Y. Yu, M. Tian, and D. Xu, "Optimized Field-Weakening Operation of PMSM Modulated Model Predictive Control Using Predictive Current Error Margin," *IEEE Transactions on Energy Conversion* 39, no. 1 (2024): 613–624.

26. Y. Dong, S. Zhang, C. Zhang, and X. Li, "Improved Parameter Robust Feedforward Formula-Based Flux-Weakening Method for Surface-Mounted Permanent Magnet Synchronous Motor," *IEEE Transactions on Transportation Electrification* 11, no. 1 (2025): 3298–3310.

27. S. Fan, Y. Zhang, J. Jin, X. Wang, and C. Tong, "Deadbeat Predictive Current Control of PMSM Drives with an Adaptive Flux-Weakening Controller," *IET Power Electronics* 15, no. 8 (2022): 753–763.

28. S. Rubino, I. R. Bojoi, E. Armando, and A. Tenconi, "Deadbeat Direct Flux Vector Control of Surface Permanent Magnet Motor Drives," *IEEE Transactions on Industry Applications* 56, no. 3 (2020): 2685–2699.

29. S. M. S. I. Shakib, D. Xiao, R. Dutta, and M. F. Rahman, "An Optimal Maximum Torque per Active Flux and Field Weakening Operation for Deadbeat Direct Torque Control Based IPMSM Drive," *IEEE Transactions on Industry Applications* 60, no. 2 (2024): 3210–3220.

30. S. Walz, R. Lazar, G. Buticchi, and M. Liserre, "Dahlin-Based Fast and Robust Current Control of a PMSM in Case of Low Carrier Ratio," *IEEE Access* 7 (2019): 102199–102208.

31. D.-H. Jang, "PWM Methods for Two-Phase Inverters," *IEEE Industry Applications Magazine* 13, no. 2 (2007): 50–61.

32. P. Cortes, J. Rodriguez, C. Silva, and A. Flores, "Delay Compensation in Model Predictive Current Control of a Three-Phase Inverter," *IEEE Transactions on Industrial Electronics* 59, no. 2 (2012): 1323–1325.

33. T.-S. Kwon and S.-K. Sul, "Novel Antiwindup of a Current Regulator of a Surface-Mounted Permanent-Magnet Motor for Flux-Weakening Control," *IEEE Transactions on Industry Applications* 42, no. 5 (2006): 1293–1300.

34. D. Zhou, L. Ding, and Y. R. Li, "Two-Stage Model Predictive Control of Neutral-Point-Clamped Inverter-Fed Permanent-Magnet Synchronous Motor Drives Under Balanced and Unbalanced DC Links," *IEEE Transactions on Industrial Electronics* 68, no. 5 (2021): 3750–3759.

35. N. Urasaki, T. Senjyu, and K. Uezato, "Investigation of Influences of Various Losses on Electromagnetic Torque for Surface-Mounted Permanent Magnet Synchronous Motors," *IEEE Transactions on Power Electronics* 18, no. 1 (2003): 131–139.

36. N. Urasaki, T. Senjyu, and K. Uezato, "A Novel Calculation Method for Iron Loss Resistance Suitable in Modeling Permanent-Magnet Synchronous Motors," *IEEE Transactions on Energy Conversion* 18, no. 1 (2003): 41–47.

37. E. Carfagna, E. Lorenzani, K. Debbadi, S. Pugliese, and M. Liserre, "Iron Losses Impact on High-Speed Drives," in *2021 IEEE Energy Conversion Congress and Exposition (ECCE)* (IEEE, 2021), 5217–5224.

17554543, 2026, 1, Downloaded from https://ietresearch.onlinelibrary.wiley.com/doi/10.1049/pel2.70318 by CochraneItalia, Wiley Online Library on [22/10/2026]. See the Terms and Conditions (https://onlinelibrary.wiley.com/terms-and-conditions) on Wiley Online Library for rules of use; OA articles are governed by the applicable Creative Commons License